Article

Pulsatory volcanism in the Main Ethiopian Rift and its environmental consequences

Check for updates

Zara Franceschini [1] ✉, Raffaello Cioni [1,2], Stéphane Scaillet[3], Gaëlle Prouteau[3], Giacomo Corti [2], Federico Sani[1,2], Alessandro Mondanaro[1], Diletta Frascerra[3], Abate A. Melaku[4,5], Bruno Scaillet[3], Clive Oppenheimer[6] & Florian Duval [3]

The East African Rift is one of Earth's largest continental landforms. It is recognized as a critical region for understanding hominin evolution yet has also undergone important transformation through ongoing tectonic and volcanic activity. An understanding of the interplay of rift kinematics, magma genesis and geomorphic evolution requires firm geochronology but this has been lacking for much of the East African Rift. Here we present detailed stratigraphic observations and high-precision $^{40}Ar/^{39}Ar$ ages for major volcanic units in the Central Main Ethiopian Rift. Our new data identify a volumetrically major episode of explosive volcanism between circa 3.85–3.42 million years ago, after aproximately 5-million years-long quiescence. Four other pulses followed but with intensity and magnitude declining over time. We suggest that the observed temporal clustering and the pulsatory volcanic activity may have influenced environmental conditions in the area, with possible implications for hominin evolution.

The East African Rift (EAR) is an ideal place to analyse the interplay between tectonic and volcanic processes during continental rifting, as it is an active magmatic rift recording different stages of extension from incipient rifting to break-up[1–3]. Being also considered the 'cradle of mankind', rift development has also been inferred to have had direct consequences on hominin evolution, given the drastic landscape modifications induced by tectonics and the intense volcanic activity[4–6] or other environmental drivers such as availability of water and wet/dry climate cycles[7–9].

Within the EAR, the Main Ethiopian Rift (MER; Fig. 1) represents an area of particular relevance to understand these rift-related processes and their possible impact on human evolution. Intense volcanic activity characterises the Miocene-recent MER evolution, as testified by several calderas or caldera-related structures and by the deposits of numerous high-volume, high-intensity explosive eruptions[10]. Previous works[5,11] identified a major pulse of explosive silicic volcanism that occurred within and adjacent to the central MER (CMER) at the end of the Middle Pleistocene, between 0.32 and 0.17 Ma (Fig. 1). It includes caldera-forming eruptions[12,13] associated with at least four volcanic complexes (Aluto, Corbetti, Shala and Gedemsa; Fig. 1) described collectively as an 'ignimbrite flare-up'[5,11,14]. Intense explosive silicic volcanism also peaked earlier in the area, at circa 3.5 Ma, with a widespread Pliocene ignimbrite, the Munesa Crystal Tuff (MCT)[10], first recognised along the eastern margin of the rift and possibly representing the largest and

most widespread event of this period. Deposits with similar lithology and stratigraphic position occur along the western rift margins (near Kella village; Fig. 1) and have been correlated with this ignimbrite, suggesting a bulk volume of 2000 km³ [10], an order of magnitude greater than the <200 km³ volume estimated for the Late Pleistocene pulse[5]. However, field and geochronologic data for the CMER include old and low-precision K/Ar determinations from the 1990s and earlier, hindering understanding of the relationship between rifting and volcanism and their potential impact on Plio-Pleistocene environmental changes and hominin evolution. Accordingly, we conducted detailed stratigraphic investigations along a 100-km-long section of the CMER, that are supported by more than fifty high-precision $^{40}Ar/^{39}Ar$ age determinations (Figs. 1, 2 and Supplementary Table 1). Our findings establish, with highly improved resolution, robust regional-scale correlations between the main volcanic units, enabling us to reassess the volcanic sequence in the context of the tectonic evolution of the CMER.

Results

Volcanostratigraphic units

The stratigraphy of the eastern margin of the CMER is dominated by three distinctive and widespread ignimbrites (MCT, Kencherra Ignimbrite and Golja Ignimbrite; Fig. 2). The oldest, the MCT *sensu strictu*

[1]Dipartimento di Scienze della Terra, Università degli Studi di Firenze, Florence, Italy. [2]Istituto di Geoscienze e Georisorse, Consiglio Nazionale delle Ricerche, Florence, Italy. [3]Institut des Sciences de la Terre d'Orléans, UMR 7327 INSU-CNRS-BRGM – Université d'Orléans, Orléans, France. [4]School of Earth Sciences, Addis Ababa University, Addis Ababa, Ethiopia. [5]School of Earth and Environmental Sciences, University of St Andrews, St Andrews, United Kingdom. [6]Department of Geography, University of Cambridge, Cambridge, United Kingdom. ✉e-mail: zara.franceschini@unifi.it
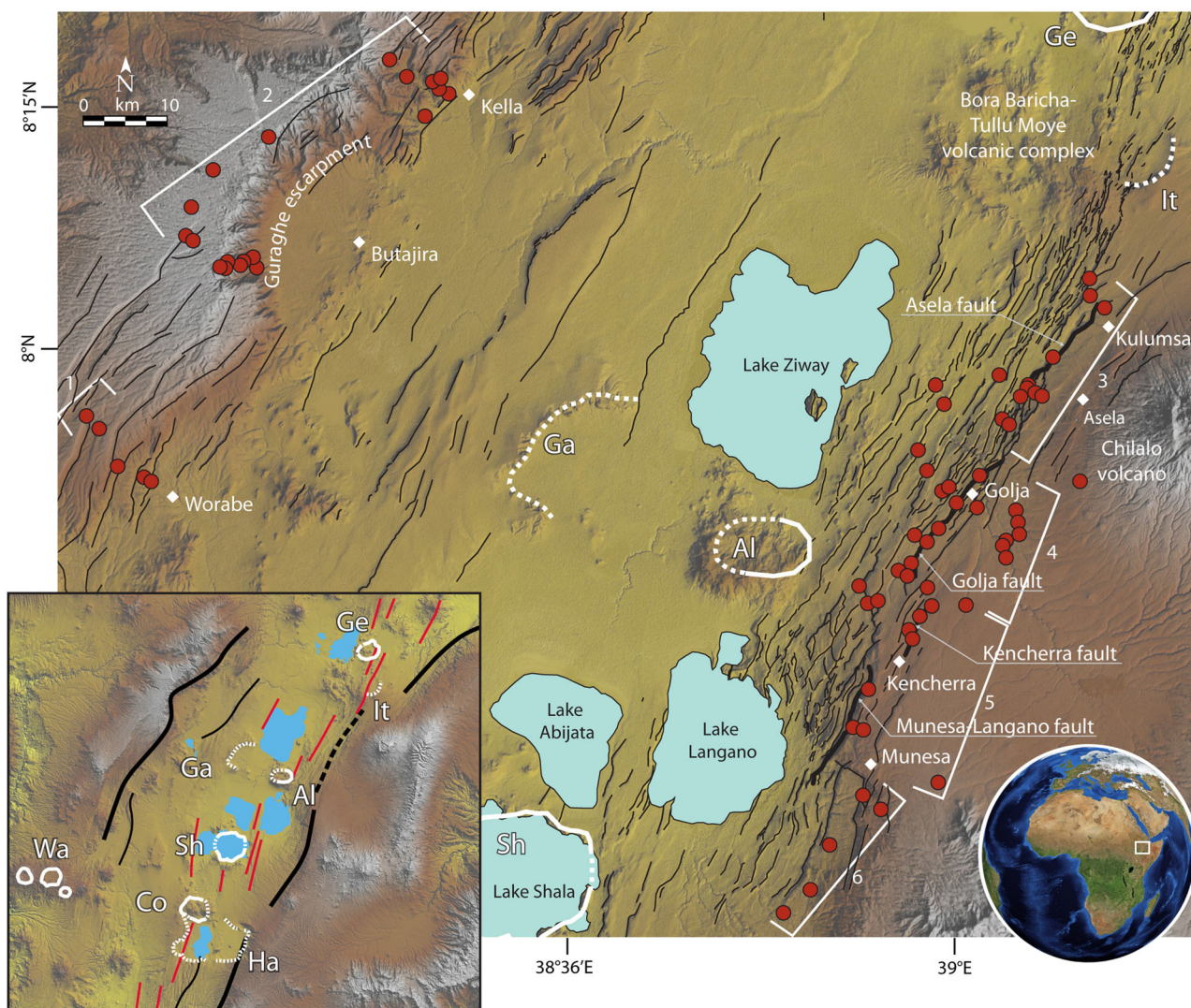
Fig. 1 | Tectonic and volcanic features of the study area. Digital Elevation Model (Shuttle Radar Topography Mission, SRTM 30 m resolution) of the CMER, with main volcanic and morphological features. Plio-Pleistocene calderas are delineated with dotted/continuous white lines as follows: It: Iteya; Ge: Gedemsa; Ga: Gademotta; Al: Aluto; Sh: Shala; Co: Corbetti; Ha: Hawassa; Wa: Wagebeta. Faults: black lines (axial faults in red in the inset). Red dots: investigated sites along the margins. White diamond: small cities/villages. Numbered white bars denote the main sectors studied for the stratigraphic reconstruction of Fig. 2.

(3.412 ± 0.004 Ma; Supplementary Table 2), is a moderately alkali-rich rhyolitic-comendite ignimbrite. It forms a 150–200 m-thick, crystal-rich deposit, increasingly welded towards its base[10], along the Munesa-Langano fault scarp (Fig. 1 and Supplementary Fig. 1a) and is found at the bottom of geothermal boreholes in the Aluto-Langano area[10,15,16]. A lithologically and compositionally similar crystal-rich ignimbrite, previously tentatively correlated with MCT[10], is exposed in cliffs of the southern part of the eastern margin (Figs. 1, 2, sect. 6). Despite the textural similarities, compositional data along with slightly older age (3.691 ± 0.007 Ma, 'H1.A' unit, Fig. 2, sect. 6 and Supplementary Table 1) show it to be a different event.

Two other early Pleistocene ignimbrites are prominent along the eastern CMER margin: the Kencherra and Golja Ignimbrites. The former (1.263 ± 0.004 Ma; Supplementary Table 2) is a high-grade[17], densely welded ignimbrite of rhyolitic composition (comendite but close to the pantellerite boundary), with a basal, metre-thick vitrophyre capped by a fiamme-bearing, thinly foliated unit, reaching 10–20 m in thickness (Supplementary Fig. 1b). It underlies the 10–30-m-thick Golja Ignimbrite (1.159 ± 0.006 Ma; Supplementary Table 2) along the eastern margin. This younger unit is variably welded, rhyolitic (pantelleritic) and grades from a basal vitrophyre to a progressively less welded facies featuring large,

rhyolitic, variably flattened white pumices and progressively enriched in black trachytic scoriae toward the top (Supplementary Fig. 1c). Smaller-scale (discontinuous) deposits of comparable age are found along both the eastern and western margins ('H6.A', 'D1.A', 'K2.A', 'K6.A' and 'I6.A' units; Supplementary Table 1). The Kencherra and Golja Ignimbrites are locally separated from the underlying MCT *s.s.* by some silicic pyroclastic units and mafic lavas and scoriae associated with nearby cinder cones (Fig. 2, sects. 3 and 4). Above the Golja Ignimbrite, on the eastern side of the CMER, several unwelded to welded, trachytic to rhyolitic ignimbrites dated between 0.76 and 0.66 Ma are more sparsely found. The youngest unit mapped there ("H3.A" unit; 0.158 ± 0.002 Ma; Supplementary Table 1 and Fig. 2, sect. 6) closes a sequence of several unwelded to densely welded ignimbrites, mostly pantelleritic in composition and younger than circa 0.30 Ma. These are found both on the rift floor and in patches on the adjacent eastern plateau.

The Plio-Pleistocene volcanic succession along the western rift margin, around Butajira village, lies upon a thick sequence of Miocene (10.2 to 9.4 Ma) subalkaline basaltic lava flows (Figs. 1, 2). The pyroclastic sequence includes a Pliocene, welded crystal-rich ignimbrite (Kella-Butajira Ignimbrite; Fig. 2, sect. 1 and Supplementary Table 2), previously correlated with the MCT of the eastern margin[10] but distinctly older (3.537 ± 0.004 Ma versus 3.412 ± 0.004 Ma).
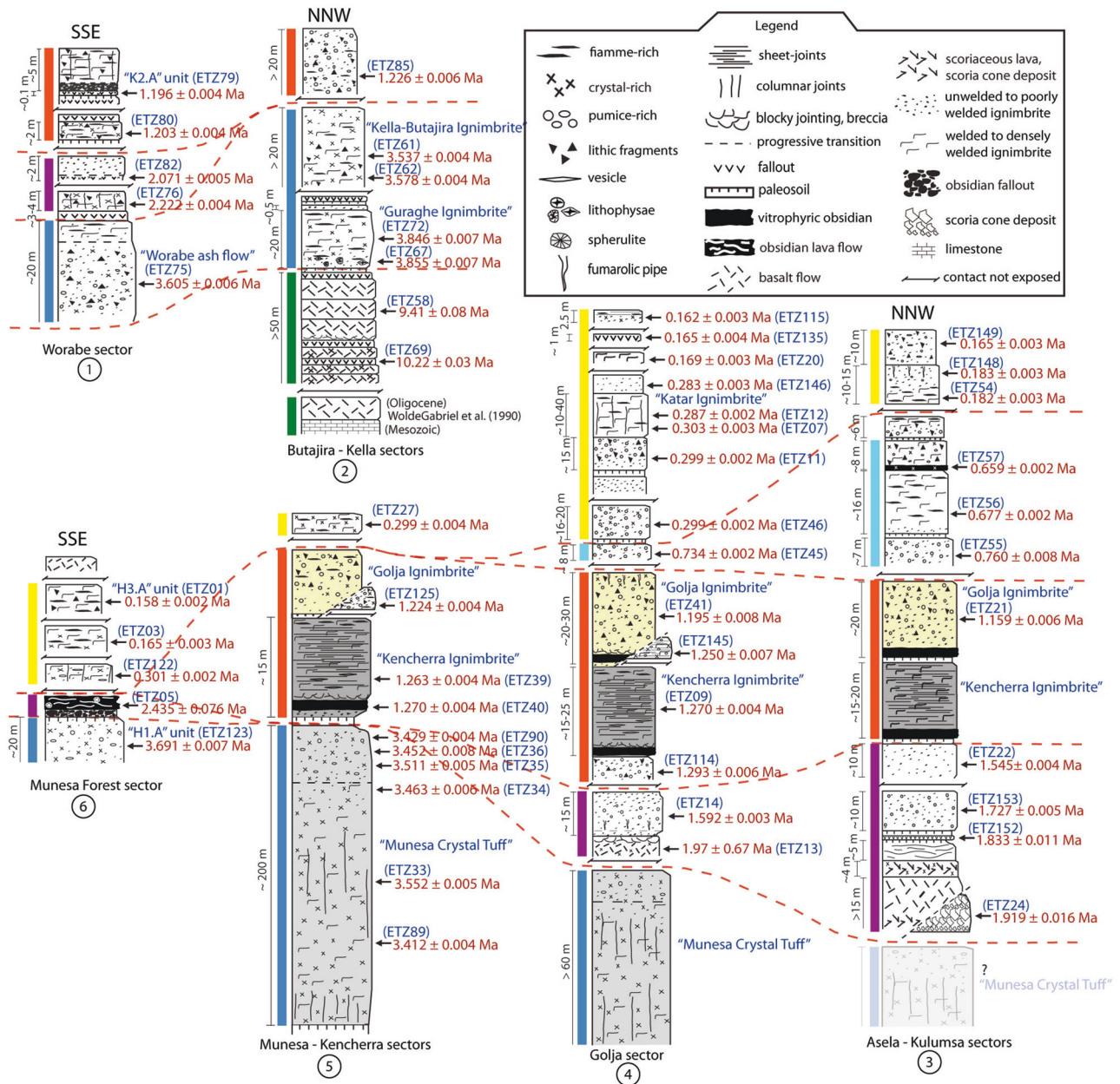
Fig. 2 | Volcanic stratigraphy and geochronology of the CMER. Composite stratigraphic columns of the western (1–2) and eastern (3–6) margins of the CMER. Dated samples are indicated by black arrows. Unit and sample names are shown in blue; the ages (below the corresponding sample) are in red. The coloured vertical bands beside stratigraphic columns identify time intervals in which the dated deposits can be grouped. Dotted red tie-lines correlate the sequences across the different sectors.

In the similar age interval, still slightly older than the MCT, we also recognise two other thick, welded or partially-welded ignimbrites (Worabe ash flow and Guraghe Ignimbrite; Fig. 2, sects. 1 and 2). At the top of the sequence, in the areas of Kella and Worabe, multiple Pleistocene pyroclastic deposits are exposed, the youngest with an age of 1.196 ± 0.004 Ma (Fig. 2, sects. 1 and 2). The Kencherra and Golja ignimbrites are not found there. The monogenetic volcanism of the Butajira Volcanic Field, dated at 0.13 Ma[18], represents the last volcanic activity in this area, and it is restricted to the rift floor.

Record of episodic volcanism
Statistical analysis (Supplementary Method 1) of our new $^{40}Ar/^{39}Ar$ dataset reveals a cyclic eruptive pattern during the past 4 Myr (Fig. 3), with all major eruptions clustered in distinct phases separated by protracted periods of quiescence or minor volcanism:

Pliocene silicic volcanism (P1, 3.85–3.41 Ma). This first phase followed about 4.6 Myr of quiescence after the emplacement of Late Miocene lava flows circa 8.5 Ma[10], which are exposed on the western margin. We identify at least five widely dispersed comenditic-rhyolite, crystal-rich units within a narrow time interval between 3.85–3.41 Ma. The predominantly welded ignimbrites are tens to hundreds of metres thick. From oldest to youngest they are the "Guraghe Ignimbrite" near Butajira, "H1.A" ignimbrite South of Munesa, "Worabe ash flow", "Kella-Butajira Ignimbrite" and "MCT s.s." (Supplementary Tables 1, 2 and Fig. 2). The source areas of these eruptions are-unknown, except for the MCT source possibly located in the Langano – Munesa area, close to the eastern margin[10]. We estimate a total bulk volume of these "Pliocene Ignimbrites" of 740–1100 km³ (580–870 km³ Dense Rock Equivalent, DRE; Fig. 3 and Supplementary Method 2 for details). Pliocene silicic products of similar age are also reported in the southern CMER (associated with
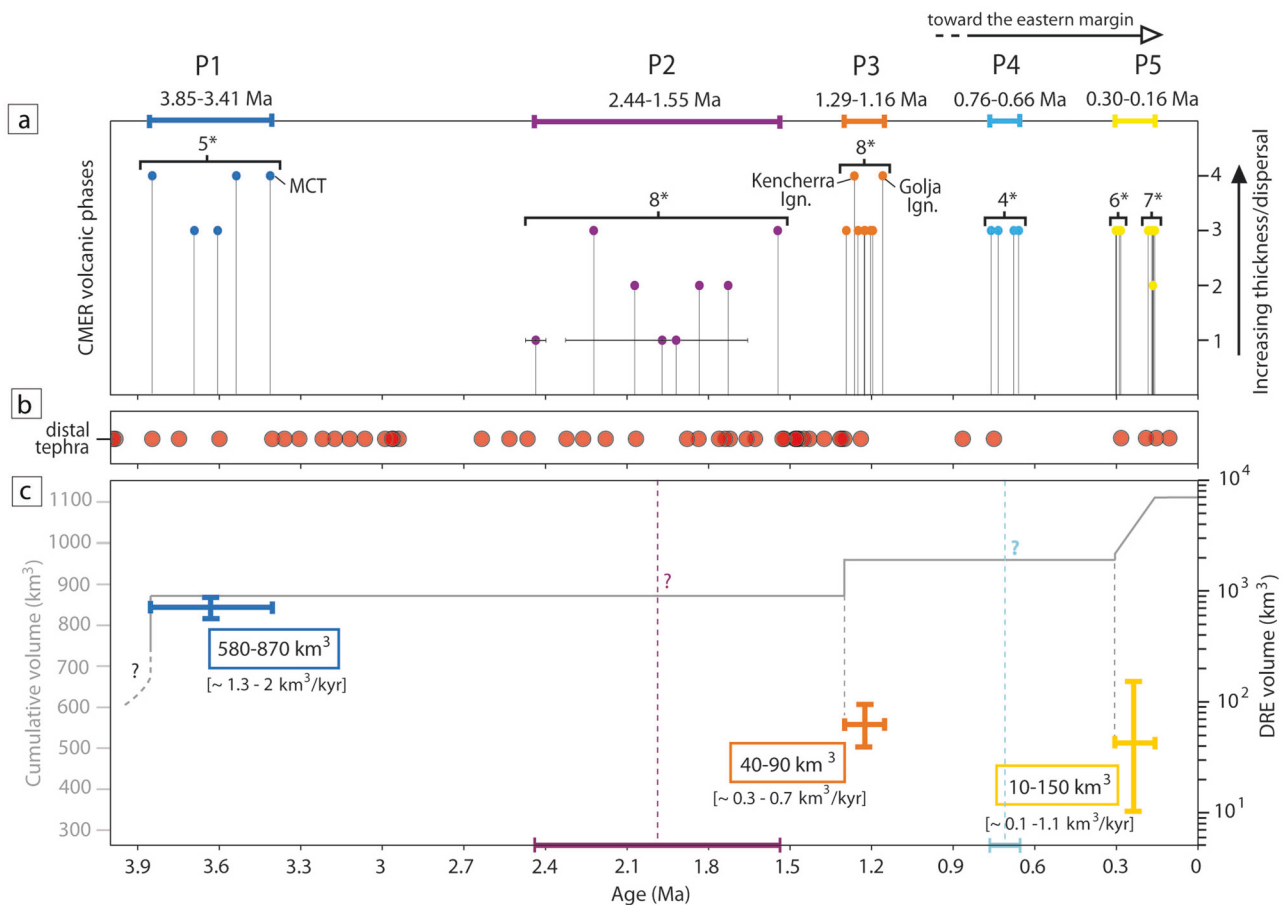
Fig. 3 | Main volcanic phases of the CMER. a The last 4 Ma of volcanism in the CMER. Four classes (grades) are distinguished (on the axis to the right) based on depositional facies, thicknesses, and dispersal (1- lava flows and scoria cone; 2- m-thick localised pyroclastic deposits; 3- unwelded to welded ignimbrites of intermediate thickness (<10 m) covering at least 15 km^2; 4- widely distributed, 15–100-m-thick, ignimbrites). #* indicates the number of units included in each phase. Age error is usually less than the corresponding symbol (except in two cases for which error bars are shown). **b** Identified ages in the distal tephra record (as discussed in Supplementary Discussion 1); the location of the distal tephra layers is shown in Supplementary Fig. 5. **c** Age-volume plot for the major volcanic clusters. The right-hand logarithmic axis represents the bulk DRE volume estimate for each cluster (vertical, coloured bars); the left-hand linear axis indicates the cumulative minimum volume (represented by the grey line). Minimum volume estimates for two phases between 2.44–1.55 Ma and 0.8–0.6 Ma cannot be constrained from the available data.

Hawassa and Wagebeta calderas)[10] and north of the investigated area (Melka Kunture)[19], suggesting that the P1 phase affected the entire CMER and that our volume estimate is a minimum (Supplementary Fig. 4).

Bimodal volcanic activity (P2, 2.44–1.55 Ma). Volcanism resumed about 1 Myr after the end of P1, with the emplacement of locally dispersed rhyolitic ash and pumice flows, and of small mafic lava flows and scoria cones dated to circa 1.9 Ma and restricted to the central-northern parts of the eastern margin (Fig. 2, sects. 3 and 4). The mafic products appear to signal the onset of a major phase of rift re-organisation associated with the development of a segmented intra-rift fault system (Wonji Fault Belt) between 2 and 1.6 Ma[10,16,20,21].

Lower Pleistocene silicic volcanism (P3, 1.29–1.16 Ma). This phase was dominated by the emplacement of the Kencherra and Golja Ignimbrites (Fig. 2), exposed along the eastern margin of the CMER only. The wide dispersal, relatively uniform thickness all along the fault scarps at different elevations, and homogeneous depositional facies of these two units suggest emplacement by pyroclastic density currents over a much less rugged topography than that of the present-day rift. Together with other less continuous deposits of age-correlative units exposed along the eastern and western margins, the cumulative volume of the products of

this phase lies between 50 and 120 km^3 (DRE volume of 40–90 km^3, Fig. 3 and Supplementary Method 2 for details).

Middle Pleistocene silicic volcanism (P4, 0.76–0.66 Ma). This includes trachytic and rhyolitic ignimbrites exposed along some sections of the main eastern boundary faults of the CMER. The lack of correlative deposits on the western margin could reflect the presence of a topographic barrier in the rift at the time of eruption, or a general shift of the emission area toward the eastern margin. The distribution of these ignimbrites is poorly constrained, precluding a meaningful estimate of their volume. However, their depositional features and discontinuous occurrence along the rift border faults suggest they record less intense and lower magnitude eruptions than those of cycles P1 and P3.

Middle-to-upper Pleistocene silicic volcanism (P5, 0.30–0.16 Ma). This phase is associated with the activity of at least four calderas (Fig. 1) inside the rift[5]. Along the eastern CMER (both on the rift floor and the eastern plateau up to 2100 m above sea level, Fig. 2), we identify deposits of this age interval that are clearly cut and offset by rift faults. $^{40}Ar/^{39}Ar$ ages define two groups, 303–280 ka (with at least six eruptions) and 183–158 ka (at least seven eruptions), separated by a ~100 kyr hiatus, so suggesting that the phase of magmatism already identified by Hutchison et al.[5] was possibly separated into two main pulses. The areal distribution

of these deposits, extended in this work to a larger sector of the eastern margin, suggests that the previous cumulative volume estimate between 10–150 km^3 for these middle-upper Pleistocene silicic deposits[5] possibly reaches into the upper end of this range.

Discussion

The detailed stratigraphic, geochronologic and petrologic study of the CMER activity demonstrates that short phases of intense and voluminous explosive activity alternated with periods of lesser and more diffuse activity. This pattern poses questions about the temporal distribution of the main phases of activity in relationship to rift evolution and kinematics. Additionally, our findings refocus attention on the significance of volcanism for understanding hominin evolution[6,22,23] (Fig. 4), on the distal tephra deposits whose dates constrain the ages of fossils, and on taphonomic biases in the fossil record.

Volumetric and petrogenetic trends over time

In parallel with the temporal clustering of major volcanic eruptions, we identify important trends in the volume and composition of magmas erupted with a clear link between the erupted magma volumes and the length of apparent quiescence between consecutive clusters. The intense, high-magnitude activity of the Pliocene phase was preceded by the longest period of quiescence (i.e. 4–5 Myr), while the subsequent ignimbrite flare-ups were characterised by shorter repose periods and reduced productivity (Fig. 3). Based on cluster durations and estimated magma volumes, the magma eruption rate for P1 ranges between 1.3–2.0 km^3 kyr^{-1} (see Methods for details), up to one order of magnitude higher than those for P3 and P5 (Fig. 3).

These rates are comparable to other ignimbrite flare-ups elsewhere[24]. The strongly evolved character of these products, possibly derived from more than 90% crystallisation of primitive basaltic magmas[25], implies that the volume of magma that arrived in the shallow magmatic system was ten times larger than the erupted material. In this assumption, a total of at least 6000–11,000 km^3 of magma were intruded in the crust of the CMER in the last 4 Myr, resulting in a minimum magma feeding rate for this period in the range 1.6–2.8 km^3 kyr^{-1} (see Methods for details). The clear transition with time toward a progressively higher peralkalinity of the most evolved products (from comendite to pantellerite), together with the smaller volumes of individual eruptions post P1 (as well as the lower eruptive rates of the following phases), likely reflect changing conditions of magma storage and crystallisation in the first 10 km of the crust[25] (progressively smaller magma reservoirs at lower temperatures). These, in turn, might be related to a general local decrease in time of the rate of magma supply (and possibly production) from the mantle, following possible changes in geodynamic processes[3] (extension rate, localisation of deformation, etc.).

Large-scale correlations and implications for volcanic evolution

The cyclic pattern of volcanism emerging from our data (Fig. 3) is consistent with the distal tephra record of large MER eruptions (Supplementary Data 1 and Supplementary Fig. 5), possibly sourced also from volcanic centres out of the CMER. A statistical analysis of the ^{40}Ar/^{39}Ar ages of these distal deposits indicates several pulses of explosive activity broadly coinciding with the CMER ^{40}Ar/^{39}Ar record (Supplementary Fig. 5). In particular, P1, the phase with eruptions of highest intensity and magnitude, correlates with a period of major tephra accumulation in the marine record between 4.0 and 3.2 Ma. It also coincides with deposition of distal tephra layers in Afar and the Turkana Basin (Supplementary Fig. 5), notably the Tulu Bor Tuff and Sidi Hakoma Tuff, that are associated with hominins and other fossils[26–29] and which had been correlated by several authors with the MCT[26–28] (Supplementary Discussion 1 and Supplementary Fig. 6).

The volcanic activity in the EARS has been commonly subdivided into large volcanic phases[30] (Supplementary Fig. 7). Detailed analysis may
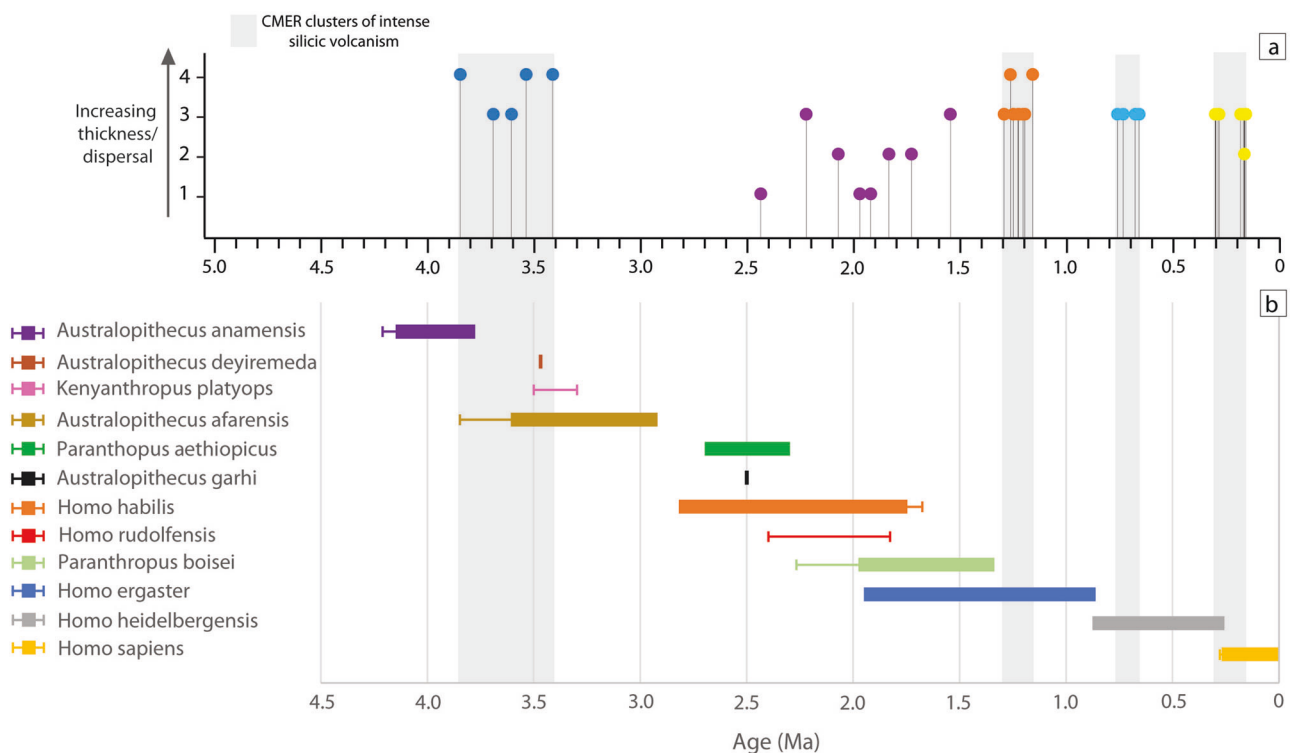

Fig. 4 | Volcanic phases in the CMER and hominin species in East Africa.
a ^{40}Ar/^{39}Ar chronogram of volcanic activity of the last 4 Myr in the CMER (this work). Vertical grey bars identify major pulses of silicic volcanism characterised by large explosive eruptions. The four classes are based on the distinction reported in Fig. 3a. **b** Age interval of key hominin species in their evolutionary context in East Africa, reconstructed as reported in Supplementary Discussion 2. Coloured horizontal bars refer to the fossil record occurring in the area nearly restricted to Ethiopia and surrounding areas. The thin lines further extend the age intervals to the whole eastern African fossil record (Supplementary Fig. 8).

document a markedly discontinuous temporal distribution of volcanic activity even within large volcanic phases, as exemplified by our high-resolution stratigraphy of the CMER revealing a pulsatory rather than a continuum pattern over the last 4 Ma (Supplementary Fig. 7). Based on our data, although it is difficult to definitively exclude the occurrence in the CMER of some volcanic activity during the inter-clusters periods, it appears that all the activity was modulated through peaks of high magma eruption rate producing large eruptions able to disperse their products up to the margins of the rift. Therefore, even though we are well aware of potential sampling bias when studying the products of a long period in a large area (e.g. we did not focus our sampling campaign on the rift floor, and thus, we may not have recorded the products of smaller eruptions sourced from this area), we can confidently affirm that our exhaustive sampling of the rift margins includes all the largest eruptions of the CMER. Investigating the products of the different sectors of the whole rift system with a high-resolution tephrochronology approach will likely refine this emerging pattern, with implications on the dynamics of rift formation, evolution and the timescales of rift-related processes[3,31–34].

Environmental perspectives

The thick, densely welded ignimbrite deposits emplaced during these temporal clusters of activity blanketed wide areas of the rift (areas in excess of 10^4 km^2). This would have had profound and immediate regional impacts on hydrological, environmental and ecological regimes, making large areas uninhabitable for prolonged times and potentially inducing hominins mobility[5,35–37]. The reduced number of hominin species in eastern Africa during the major clusters of intense activity (Fig. 4) could bear witness of this correlation. In particular, our data suggest that most hominins speciation took place during a period of low intensity, low volume, volcanic activity (P2, Fig. 4), whereas some moments of relevant species turnover within the hominins lineage coincide with periods of high volcanic activity (Fig. 4 and Supplementary Discussion 2). These local, immediate effects of volcanic activity may have been compounded by global-scale climatic perturbations associated with emissions of large quantities of sulphur and halogens into the stratosphere. We estimate that each individual episode of the Pliocene cluster (P1) could have released around 200 Tg of sulphur (Supplementary Discussion 3), over 20 times greater than that released into the stratosphere by the 1991 eruption of Mt. Pinatubo[38,39]. Although these estimations are affected by large uncertainty also in the most favourable cases[40], only a few events of comparable sulphur yield are recorded in ice cores spanning the Holocene[41]. Future modelling studies should thus explore how several mega eruptions occurring in a row during a time interval of 10^4-10^5 years may have led to global climate disruption in the Pliocene.

Our new scheme of time distribution of CMER volcanism provides a robust template for a careful re-evaluation of its geological and environmental evolution, also suggesting that this kind of approach, if reproduced at the scale of the whole rift, could reveal important processes up to now obscured by the still low-resolution of the available chronostratigraphic data.

Methods

Fieldwork and sampling

Since one of the main goals is to study the long-term distribution of volcanism in the CMER from its early stage of rifting in the Pliocene and considering that the rift floor is mainly covered by the products of the Pleistocene-Holocene volcanism and lacustrine deposits, we conducted two field surveys in 2019 and 2020 focusing on the eastern and western margins of the rift, which allow the observation also of the older volcanic products. Field campaigns were mainly based on the collection of geological-structural data, the study of the different deposits observed and the sampling of a large number of volcanic rocks. In total, 163 samples have been collected (Supplementary Data 3), mostly from ignimbrites and, to a minor extent, from lava flows and pyroclastics…, etc. Samples were collected on most of the volcanic units recognised in the field from different outcrops and, where possible, from the same outcrop at different stratigraphic positions within a

single unit, in order to characterise its vertical facies variation. To each distinct volcanic deposit, we assigned a unit name (Supplementary Data 3) indicative of the sampling site and stratigraphic position within the outcrop (e.g., the outcrop at site A1 presents four overlaying volcanic units which are named, from the bottom to the top, 'K1.A', 'K1.B', 'K1.C' and 'K1.D'). When outcrops of the same deposit are observed in multiple investigated sites, the unit takes the name of the site where it has been first observed or from the toponym where it is best exposed. The general term 'ignimbrite' is intended as the deposit (whether welded or not) of pyroclastic density currents (PDC) formed during large explosive eruptions[42–44]. Other lithological terms (ash flow, pumice flow…, etc.) were used to describe minor PDC deposits locally found in the different stratigraphic sections.

The eastern and western margins were divided into sectors (each area comprehensive of multiple investigated sites), and for each one, we reconstructed a composite stratigraphic column by considering the volcanic stratigraphy observed at the investigated sites (i.e. the occurrence marker beds defined by diagnostic features, facilitate identification and allow tracing correlations) and by integrating this information with geochronological data where the volcanic units do not occur in stratigraphic succession. Composite stratigraphic columns are reconstructed without considering faults but simply reporting in stratigraphical order the volcanic succession occurring in each area.

^{40}Ar/^{39}Ar dating

In order to build a comprehensive geochronological database, 55 samples were selected from different outcrops and from the same ignimbrite units recognised in different areas to validate correlations based on lithological, sedimentological, and compositional data. Vertically extensive sampling was also conducted all over the investigated area across multiple stratigraphic sections, including at different elevations within the same deposit, to check for internal ^{40}Ar/^{39}Ar variations in connection with depositional facies. Stringent criteria of freshness were applied, focusing on porphyritic samples of all main volcanic successions exposed at the rift margins. Samples were crushed, sieved to 250–500 μm and 500–1000 μm size fraction before ultrasonic cleaning in water. Sanidine grains were handpicked under a binocular microscope from ignimbrites, pumices, and fallout deposits. Plagioclase crystals were also extracted from a phaneritic basalt flow, and glass fragments and matrix grains were obtained from an obsidian rhyolitic lava flow, a scoria and an aphyric basalt flow (for the latter two samples the groundmass grains were selected among the grain size 250–500 μm). Crystals were leached in 5% HF to remove adhering glass. Glass and groundmass grains were etched in 5 and 20% HNO_3, respectively. All samples were finally thoroughly rinsed and ultrasonically cleaned in water.

Samples and fluence monitor standards were packaged in Al foil, stacked in Al tubes and irradiated in the CLICIT Cd-lined slot of Corvallis Nuclear Reactor (Oregon State University, United States). Sanidines of the Fish Canyon Tuff (FCs), with an age of 28.02 ± 0.28 Ma[45], were used to monitor ^{39}Ar production during irradiation and determine the irradiation parameters (J) (Supplementary Data 4). ^{40}Ar/^{39}Ar experiments were conducted at the Argon facility at ISTO featuring three high-resolution Helix SFT mass-spectrometer operated with a mass resolution in excess of 750. Each of these is outfitted to a CO_2-laser- based extraction system featuring ultra-low argon blanks. Gas was extracted from the irradiated crystals via total fusion, while step-heating incremental heating was applied to generate apparent age spectra for groundmass and glass fragments. The extracted gas was purified through exposure to a cooling U-trap of liquid Nitrogen (held at around −130 °C) and two hot GP50 SAES getters before admission into the mass-spectrometer. Isotopic data (Supplementary Data 4) are regressed and corrected for instrumental parameters (blank, mass discrimination, dead-time, post-irradiation decay and atmospheric contamination) according to procedures and the error sensitivity analysis described in detail elsewhere[46]. 'Empty' line blanks were monitored between each consecutive gas admission and interpolated to correct the intervening samples across the analytical session on a daily basis. Ages and errors for each sample (with an average of 20 analyses per sample) are pooled as a weighted mean age

(WMA) to estimate the best age and error. The WMA is calculated over the analyses sorted by age, starting with the first (youngest) age and pooling the data in sequence until the MWSD exceeds the two-sided 0.95 fiducial intervals predicted from χ^2 statistics for n-1 degree of freedom. The MSWD (mean squared weighted deviation) is a measure of the data scatter relative to analytical precision, and it is used to test the internal consistency of the pooled data. Final ages are reported with ±1 s error.

Volume and rate estimations

The volume estimation of the deposits involved in the intense silicic volcanic clusters are obtained by considering the areal dispersion of the products and the thicknesses observed at the investigated sites (Supplementary Fig. 4). The volume is estimated as the volume of the 3D Delaunay triangulation (obtained using a dedicated MatLab routine) on the points of thickness defined. The dense rock equivalent (DRE) volume is determined by considering an average density of $1800\ kg\,m^{-3}$ as representative of these densely welded to poorly welded ignimbrites[47], and a melt density of $2300\ kg\,m^{-3}$ for the rhyolitic magma[48,49]. These volume estimates, divided by the age interval of each cluster, were then used to determine the magma eruption rate.

Moreover, assuming a 90% fractionation of basaltic magmas to produce the final rhyolitic compositions[25], we estimate that the volume of magma entered in the crust to produce these products was at least ten times higher. The magma feeding rate is estimated by dividing the DRE volume of the magma entered in the system by the total duration of the quiescence and activity periods (4 Ma).

Melt inclusions study

For melt inclusion analysis, samples were first granulated and sieved. The grain size classes 0.25–0.5 mm and 0.5–1 mm were ultrasonically rinsed in water to remove all the residual powder particles, dried in the oven, and then observed under the binocular microscope to separate crystals containing well-preserved melt inclusions. Melt inclusions embedded within quartz were preferred due to the better preservation of this mineral, but in some cases, well-preserved melt inclusions were also found in sanidine and, occasionally, in plagioclase. An average of 15 crystals was selected from each sample, each of them embedding one or several melt inclusions. Each crystal was separately embedded in Vertex Orthoplast resin by using Thovertex solvent and, once hardened, singularly polished down with Al_2O_3 powders and polishing papers of progressively lower granulometry to a fine grade up to 1 μm. All crystals with exposed and polished melt inclusion belonging to the same sample were carefully removed from resin (via heating) and embedded together in a mount of epoxy resin with the polished surface exposed. The mounts were observed under the binocular microscope and carbon-coated for analyses.

Selected crystals of the three marker beds (specifically, ETZ31 and ETZ90 from the MCT, ETZ30 from the Kencherra Ignimbrite and ETZ136 from the Golja Ignimbrite) were first inspected with SEM for image collection and melt inclusions mapping, then analysed for major element and volatile concentrations with an Electron Micro Probe analyzer (EMPA) housed at the laboratories of the Institut des Sciences de la Terre d'Orléans, in France.

It was not always possible to analyse all the melt inclusions, due to their size (below the minimum value of 20 μm), fracturing or other analytical issues, but, for each sample, the number of melt inclusions analysed was between 11 and 21.

The melt inclusions were analysed by a Cameca SX Five during three EMPA sessions together with standards of rhyolitic composition with four different water concentrations (0, 2.42, 4.24 and 6.38%, as measured with Karl Fisher Titration[50]) as a reference for Na-loss correction and water content estimation of the studied melt inclusions. About three or four analyses were done on each melt inclusion and the results were averaged to obtain a mean value and related standard deviation. Major elements and volatile concentrations for melt inclusions are shown in Supplementary Data 2, where the average value of each melt inclusion has been corrected for

alkali loss and normalised to 100%. To correct the measured concentrations for alkali loss, we multiply the measured raw Na_2O wt.% (averaged among the analyses performed on a single inclusion) by a Correction Factor (CF). The value of CF was obtained by analysing the glass rhyolitic standards and dividing the known Na_2O content (3.29 wt%)[50] by the measured Na_2O concentration. The difference between the corrected and raw Na_2O contents is then added to the averaged total. We then use this corrected total to normalise to 100% the other major element concentrations. H_2O contents were estimated by comparing the hydrous total corrected for alkali loss (averaged among the analyses of a single inclusion) to the raw totals yielded by the analysed standards (the raw total of each standard is averaged among the four analyses performed on the same standard of known water content). The raw totals of the four standards are plotted against their corresponding water content obtaining a linear correlation relative to the total-H_2O content relation. The same equation was applied to the corrected hydrous total of the melt inclusions to obtain an estimation of their water content[51,52]. The same procedure was applied to partially recrystallised melt inclusions taking care to avoid the recrystallised rim and focusing on the glassiest portion of the melt inclusion. Completely recrystallised melt inclusions were not considered for analyses.

Data availability

All data needed to evaluate the conclusions in the paper are present in the paper and/or the Supplementary Information. Further geochronological and geochemical data in support to this study can be found in the Zenodo online repository (https://doi.org/10.5281/zenodo.12750599)[52].

References

1. Hayward, N. J. & Ebinger, C. J. Variations in the along-axis segmentation of the Afar Rift system. *Tectonics* **15**, 244–257 (1996).
2. Ebinger, C. J. Continental break-up: the East African perspective. *Astron. Geophys.* **46**, 2–16 (2005).
3. Corti, G. Continental rift evolution: from rift initiation to incipient break-up in the Main Ethiopian Rift, East Africa. *Earth Sci. Rev.* **96**, 1–53 (2009).
4. WoldeGabriel, G. et al. in *Volcanic Hazards and Disasters in Human Antiquity* (Geological Society of America, 2000).
5. Hutchison, W. et al. A pulse of mid-Pleistocene rift volcanism in Ethiopia at the dawn of modern humans. *Nat. Commun.* **7**, 1–12 (2016a).
6. Olaka, L. & Ebinger, C. J. Tectonic and Paleoclimatic setting for hominin evolution in eastern Africa. *Elements* **19**, 82–87 (2023).
7. Bailey, G. N. & King, G. C. Dynamic landscapes and human dispersal patterns: tectonics, coastlines, and the reconstruction of human habitats. *Quat. Sci. Rev.* **30**, 1533–1553 (2011).
8. Maslin, M. A. et al. East African climate pulses and early human evolution. *Quat. Sci. Rev.* **101**, 1–17 (2014).
9. Cuthbert, M. O. et al. Modelling the role of groundwater hydro-refugia in East African hominin evolution and dispersal. *Nat. Commun.* **8**, 15696 (2017).
10. WoldeGabriel, G., Aronson, J. L. & Walter, R. C. Geology, geochronology, and rift basin development in the central sector of the Main Ethiopia Rift. *Geol. Soc. Am. Bull.* **102**, 439–458 (1990).
11. Mohr, P., Mitchell, J. G. & Raynolds, R. G. H. Quaternary volcanism and faulting at O'a Caldera, Central Ethiopian Rift. *Bull. Volcanol.* **43**, 173–189 (1980).
12. McNamara, K. et al. Using lake sediment cores to improve records of volcanism at Aluto volcano in the Main Ethiopian Rift. *Geochem. Geophys. Geosyst.* **19**, 3164–3188 (2018).
13. Vidal, C. M. et al. Geochronology and glass geochemistry of major pleistocene eruptions in the Main Ethiopian Rift: towards a regional tephrostratigraphy. *Quat. Sci. Rev.* **290**, 107601 (2022b).

14. Peccerillo, A. et al. Relationships between mafic and peralkaline silicic magmatism in continental rift settings: a petrological, geochemical and isotopic study of the Gedemsa volcano, central Ethiopian rift. *J. Petrol.* **44**, 2003–2032 (2003).

15. Teklemariam, M., Battaglia, S., Gianelli, G. & Ruggieri, G. Hydrothermal alteration in the Aluto-Langano geothermal field. *Ethiop. Geotherm.* **25**, 679–702 (1996).

16. Hutchison, W. et al. The eruptive history and magmatic evolution of Aluto volcano: new insights into silicic peralkaline volcanism in the Ethiopian rift. *J. Volcanol. Geotherm. Res.* **328**, 9–33 (2016b).

17. Walker, G. P. L. Ignimbrite types and ignimbrite problems. *J. Volcanol. Geotherm. Res.* **17**, 65–88 (1983).

18. Rooney, T. O., Furman, T., Yirgu, G. & Ayalew, D. Structure of the Ethiopian lithosphere: xenolith evidence in the Main Ethiopian Rift. *Geochim. Cosmochim. Acta* **69**, 3889–3910 (2005).

19. Salvini, R., Riccucci, S. & Francioni, M. Topographic and geological mapping in the prehistoric area of Melka Kunture (Ethiopia). *J. Maps* **8**, 169–175 (2012).

20. Kazmin, V. Geodynamic control of rift volcanism. *Geol. Rundsch.* **69**, 757–769 (1980).

21. Boccaletti, M. et al. Quaternary oblique extensional tectonics in the Ethiopian Rift (Horn of Africa). *Tectonophysics* **287**, 97–116 (1998).

22. Basell, L. S. Middle Stone Age (MSA) site distributions in eastern Africa and their relationship to quaternary environmental change, refugia and the evolution of *Homo sapiens*. *Quat. Sci. Rev.* **27**, 2484–2498 (2008).

23. Bailey, G. N., Reynolds, S. C. & King, G. C. Landscapes of human evolution: models and methods of tectonic geomorphology and the reconstruction of hominin landscapes. *J. Hum. Evol.* **60**, 257–280 (2011).

24. de Silva, S. L. & Gosnold, W. D. Episodic construction of batholiths: insights from the spatiotemporal development of an ignimbrite flare-up. *J. Volcanol. Geotherm. Res.* **167**, 320–335 (2007).

25. Scaillet, B. & Macdonald, R. Phase relations of peralkaline silicic magmas and petrogenetic implications. *J. Petrol.* **42**, 825–845 (2001).

26. Walter, R. C. & Aronson, J. L. Age and source of the Sidi Hakoma tuff, Hadar formation, Ethiopia. *J. Hum. Evol.* **25**, 229–240 (1993).

27. White, T. D. et al. New discoveries of Australopithecus at Maka in Ethiopia. *Nature* **366**, 261–265 (1993).

28. WoldeGabriel, G. et al. The role of tephra studies in African paleoanthropology as exemplified by the Sidi Hakoma Tuff. *J. Afr. Earth Sci.* **77**, 41–58 (2013).

29. Villaseñor, A., Bobe, R. & Behrensmeyer, A. K. Middle Pliocene hominin distribution patterns in Eastern Africa. *J. Hum. Evol.* **147**, 102856 (2020).

30. Rooney, T. O. The Cenozoic magmatism of East Africa: part II–rifting of the mobile belt. *Lithos* **360**, 105291 (2020).

31. Bonini, M. et al. Evolution of the Main Ethiopian Rift in the frame of Afar and Kenya rifts propagation. *Tectonics* **24**, https://doi.org/10.1029/2004TC001680 (2005).

32. Keranen, K. & Klemperer, S. L. Discontinuous and diachronous evolution of the Main Ethiopian Rift: implications for development of continental rifts. *Earth Planet. Sci. Lett.* **265**, 96–111 (2008).

33. Mazzarini, F., Le Corvec, N., Isola, I. & Favalli, M. Volcanic field elongation, vent distribution, and tectonic evolution of a continental rift: the Main Ethiopian Rift example. *Geosphere* **12**, 706–720 (2016).

34. Ebinger, C., van Wijk, J., Olaka, L., Mériaux, C. & Fontijn, K. All scales must be considered to understand rifts. *Nat. Rev. Earth Environ.* **4**, 209–210 (2023).

35. Fedele, F. G., Giaccio, B., Isaia, R. & Orsi, G. Ecosystem impact of the Campanian ignimbrite eruption in Late Pleistocene Europe. *Quat. Res.* **57**, 420–424 (2002).

36. Self, S. The effects and consequences of very large explosive volcanic eruptions. *Philos. Trans. R. Soc. A: Math. Phys. Eng. Sci.* **364**, 2073–2097 (2006).

37. Cassidy, M. & Mani, L. Prepare now for big eruptions. *Nature* **608**, 469–471 (2022).

38. Bluth, G. J., Doiron, S. D., Schnetzler, C. C., Krueger, A. J. & Walter, L. S. Global tracking of the SO2 clouds from the June, 1991 Mount Pinatubo eruptions. *Geophys. Res. Lett.* **19**, 151–154 (1992).

39. Westrich, H. R. & Gerlach, T. M. Magmatic gas source for the stratospheric SO2 cloud from the June 15, 1991, eruption of Mount Pinatubo. *Geology* **20**, 867–870 (1992).

40. Pouget, M., Moussallam, Y., Rose-Koga, E. F. & Sigurdsson, H. A reassessment of the sulfur, chlorine and fluorine atmospheric loading during the 1815 Tambora eruption. *Bull. Volcanol.* **85**, 66 (2023).

41. Sigl, M., Toohey, M., McConnell, J. R., Cole-Dai, J. & Severi, M. Volcanic stratospheric sulfur injections and aerosol optical depth during the Holocene (past 11 500 years) from a bipolar ice-core array. *Earth Syst. Sci. Data* **14**, 3167–3196 (2022).

42. Walker, G. P. Grain-size characteristics of pyroclastic deposits. *J. Geol.* **79**, 696–714 (1971).

43. Sparks, R. S. J., Self, S. & Walker, G. P. Products of ignimbrite eruptions. *Geology* **1**, 115–118 (1973).

44. Brown, R. J. & Andrews, G. D. in *The Encyclopedia of Volcanoes* (Academic Press, 2015).

45. Renne, P. R. et al. Intercalibration of standards, absolute ages and uncertainties in 40Ar/39Ar dating. *Chem. Geol.* **145**, 117–152 (1998).

46. Scaillet, S. Numerical error analysis in 40Ar/39Ar dating. *Chem. Geol.* **162**, 269–298 (2000).

47. Quane, S. L. & Russell, J. K. Ranking welding intensity in pyroclastic deposits. *Bull. Volcanol.* **67**, 129–143 (2005).

48. Lesher, C. E. & Spera, F. J. in *The Encyclopedia of Volcanoes* (Academic Press, 2015).

49. Iddon, F. & Edmonds, M. Volatile-rich magmas distributed through the upper crust in the Main Ethiopian Rift. *Geochem. Geophy. Geosyst.* **21**, e2019GC008904 (2020).

50. Scaillet, B. & Evans, B. W. The 15 June 1991 eruption of Mount Pinatubo. I. Phase equilibria and pre-eruption P–T–f O2–f H2O conditions of the dacite magma. *J. Petrol.* **40**, 381–411 (1999).

51. Di Carlo, I., Pichavant, M., Rotolo, S. G. & Scaillet, B. Experimental crystallization of a high-K arc basalt: the golden pumice, Stromboli volcano (Italy). *J. Petrol.* **47**, 1317–1343 (2006).

52. Franceschini, Z. et al. Geochronological and geochemical data of volcanic deposits of the Central Main Ethiopian Rift. *Zenodo* https://doi.org/10.5281/zenodo.12750599 (2024).

Acknowledgements

Author contributions

R.C., G.C., F.S., Z.F., B.S., S.S., G.P., D.F. and A.A.M. took part in field campaigns and data collection in Ethiopia and A.A.M. was essential in facilitating the fieldwork. The interpretation and reconstruction of the volcanic stratigraphy of the area was done by Z.F., R.C., G.C., F.S, S.S. and B.S. Z.F. and D.F. prepared the samples and conducted $^{40}Ar/^{39}Ar$ dating; S.S. and F.D. kept the Argon lab running, supervised the irradiation, cycling of the samples, the $^{40}Ar/^{39}Ar$ analysis and performed the $^{40}Ar/^{39}Ar$ calculations along with the data interpretation. Z.F. prepared the samples for geochemical analysis and conducted the melt inclusions study under the supervision of R.C., B.S. and G.P.; Z.F., R.C. B.S. and G.P. contributed to the interpretation of the results. Z.F. prepared the first draft of the manuscript

Competing interests

Additional information